

Optimal Decoupled Disturbance Observers for Dual-input Single-output Systems

Xu Chen

Department of Mechanical Engineering
University of California, Berkeley
California, 94720, USA
Email: maxchen@me.berkeley.edu
xuchen@cal.berkeley.edu

Masayoshi Tomizuka

Department of Mechanical Engineering
University of California, Berkeley
California, 94720, USA
Email: tomizuka@me.berkeley.edu

The disturbance observer (DOB) has been a popular robust control approach for servo enhancement in single-input single-output systems. This paper presents a new extension of the DOB idea to dual- and multi-input single-output systems, and discusses an optimal filter design technique for the related loop shaping. The proposed decoupled disturbance observer (DDOB) provides the flexibility to use the most suitable actuators for compensating disturbances with different spectral characteristics. Such a generalization is helpful, e.g., for modern dual-stage hard disk drives, where enhanced servo design is becoming more and more essential in the presence of vibration disturbances.

keywords: MISO systems, dual-stage hard disk drives, disturbance observer, audio vibration, optimal filter design

Nomenclature

DDOB	decoupled disturbance observer
G_{yd}	transfer function from d to y
$S(z^{-1})$	sensitivity function (output disturbance-rejection function)

1 Introduction

Practical systems are inevitably subjected to external disturbances and model variations. One robust control approach for servo enhancement is to apply the disturbance observer (DOB) [1], which counteracts the effects of external disturbances and model uncertainties by estimating a lumped equivalent input disturbance. As a flexible and powerful add-on element for servo enhancement, DOB has been applied in broad control

applications, including but not limited to: hard disk drives [2,3], optical disk drives [4], linear motors [5], positioning tables [6], robot arms [7], and automotive engines [8].

The central concept of the disturbance observer is that, if the plant dynamics can be properly inverted, then the equivalent input disturbance can be extracted from the control signal and the plant output. This design principle has clear intuitions for single-input single-output (SISO) systems. However, for dual-input single-output (DISO), and more generally multi-input single-output (MISO) systems, the situation is more complex, and the generalization of DOB has not been fully addressed. The main difficulty here is that, there are multiple control inputs while only one combined output signal is measured. It becomes nontrivial to generate the disturbance estimate for each control channel using just the combined output. It also remains unclear how the compensation effort should be distributed to each actuator, as the disturbance information is coupled with the multi-channel control commands in the measured output.

In [9], one conventional DOB was applied to each channel in a dual-stage hard disk drive (HDD). The coupling effects between the two channels were treated as internal disturbances in individual DOBs, and a coupled frequency-domain inequality was proposed for DOB tuning. References [10] and [11] discussed state-space designs to implement the DOB idea in special classes of nonlinear MIMO systems. The transfer-function approach of model inversion was replaced with an observer-type state-space construction. More specifically, [11] utilized the structure of an extended

state observer (ESO) and active disturbance rejection control (ADRC) to reject the coupling effects as internal disturbances; [10] analyzed the importance of MIMO disturbance observers, and constructed a linear-matrix-inequality-based state-space disturbance observer for a special class of nonlinear MIMO system. In these related literatures, a customized treatment of MISO systems was not given. Independent application of each actuator for disturbance rejection (decoupled disturbance compensation) remains as an unaddressed issue.

In this paper, we discuss a new decoupled disturbance observer (DDOB) to address the nontrivial model inversion and the coupled disturbance rejection problem in MISO systems. Different from the previous literatures, we focus on the separation between the external disturbances and the internal control actions. This enables the obtaining of a partial-inverse based disturbance-rejection scheme, where no cross-channel coupling effects enter as internal disturbances, and designers have the flexibility to distribute the compensation effort according to the mechanical properties of each actuator as well as the disturbance characteristics. These features make DDOB especially beneficial for rejecting disturbances that consist of energy components at different frequency ranges, where it is ideal for each actuation channel to be flexibly adjusted for customized servo enhancement.

Another contribution of the paper is to provide a convex-optimization-based band-pass filter design method in (D)DOB schemes. Compared to the low-pass or narrow-band filter designs [3, 12–14], one main new feature of the algorithm is the flexibility to arbitrarily constrain the magnitude upper bound of the filter, and in the meantime directly minimize the maximum amplification in the feedback sensitivity function. This makes the algorithm particularly helpful for the rejection of vibrations with wide spectral peaks, which has become a central problem in HDD applications (more details in Section 2).

In the remainder of the paper, we first provide the background of DDOB design in Section 2, then present the structure of DDOB and its time-domain intuition in Section 3. Sections 4 and 5 provide the stability condition and the proposed loop-shaping criteria. Following that, Section 6 presents the related filter design techniques. Sections 7 and 8 provide, respectively, a reduced-order implementation of DDOB and several case studies. Finally, Section 9 concludes the paper. A short version of the paper was presented in [15]. The present paper is a substantially extended version that provides detailed proofs and derivations (in Sections 2, 3, and 4), newly developed extensions (in Sections 1, 3.4, 6, and 7), and implementation details (Section 8).

2 Dual-Stage Hard Disk Drives

One practical motivation of DDOB design is in the control of hard disk drive (HDD) systems. With the

ever increasing demand of larger capacity in HDDs, piezoelectric-based dual-stage actuation has become an essential technique to break the bottleneck of the servo performance in single-actuator HDDs [16, 17]. In this enhanced mechanical configuration, a microactuator (MA) is mounted on a conventional Voice Coil Motor (VCM) actuator, for accurate positioning of the read/write heads that are equipped at the end of MA (see Fig. 1). The VCM actuator has a larger range of movement, providing coarse motion for the position servo. The MA has a limited range of movement but provides faster and finer positioning. Compared to the VCM actuator, the MA has enhanced mechanical performance in the high-frequency region, providing the capacity to greatly increase the servo bandwidth and disturbance-attenuation capacity. In this DISO system, the two actuators receive respectively current and voltage inputs, while only the position error of the read/write head is measurable for servo control.

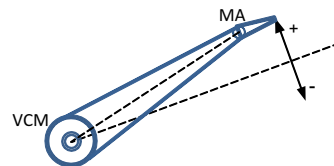


Fig. 1: Mechanical structure of a dual-stage HDD

A great challenge in HDD control is the strong external disturbance caused by, e.g., audio vibrations. Attenuation of this type of vibrations has become essential in modern HDDs, as high-power speakers in multimedia applications (such as all-in-one computers and digital TVs) generate a significant amount of external disturbances to the HDD. Such vibrations are extremely difficult to handle in a cost-effective way due to their intrinsic properties of (a) environmental dependence; (b) appearing in a wide frequency range (from 300 Hz to as high as 4 kHz); and (c) having multiple resonances and wide spectral peaks.

3 DDOB Structure: Open-loop Configuration

Consider a sampled-data linear time-invariant DISO system $P(z^{-1}) = [P_1(z^{-1}), P_2(z^{-1})]$, with the input-output relation:

$$y(k) = P_1(z^{-1})u_1(k) + P_2(z^{-1})u_2(k) + d(k). \quad (1)$$

Here $y(k)$, $u_i(k)$ ($i = 1, 2$) and $d(k)$ represent respectively the plant output, the plant inputs, and the lumped external disturbance. We will use the notation $P_i(z^{-1})$ to denote both the transfer function and the pulse transfer function (where z^{-1} is a delay operator satisfying $z^{-1}u(k) = u(k-1)$), so that $P_i(z^{-1})u_i(k)$ can

represent the time-domain output of $P_i(z^{-1})$.

Remark: Without loss of generality, Eq. (1) models the external disturbance as a lumped signal at the plant output. The input disturbances are absorbed in $d(k)$ by

$$d(k) = d_o(k) + P_1(z^{-1})d_1(k) + P_2(z^{-1})d_2(k) \quad (2)$$

where $d_o(k)$ and $d_i(k)$ are, respectively, the actual output and input disturbances. We place no assumption on the statistical properties of the disturbance. The derivations in the remainder of the paper apply to both stationary and non-stationary $d(k)$'s.

Fig. 2 shows the structure of the proposed DDOB for the second channel $P_2(z^{-1})$. Throughout the paper, we denote $\hat{P}_i(z^{-1})$ as the nominal model of $P_i(z^{-1})$, and let m_i be the relative degree of $\hat{P}_i(z^{-1})$. In this way, although $\hat{P}_2^{-1}(z^{-1})$ may not be realizable, $z^{-m_2}\hat{P}_2^{-1}(z^{-1})$ in Fig. 2 is proper and implementable.

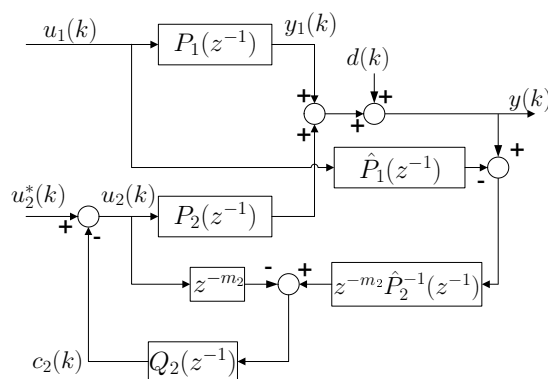


Fig. 2: Block diagram of DDOB for $P_2(z^{-1})$

3.1 Time-domain Disturbance-rejection Criteria

The idea of DDOB is to apply the compensation signal $c_2(k)$ to $P_2(z^{-1})$, such that the overall lumped disturbance $d(k)$ is compensated. To see this, note that from Fig. 2, the output of $Q_2(z^{-1})$ is given by

$$c_2(k) = Q_2(z^{-1}) \left[z^{-m_2} \hat{P}_2^{-1}(z^{-1}) (y(k) - \hat{P}_1(z^{-1})u_1(k) - z^{-m_2}u_2(k)) \right], \quad (3)$$

which is equivalent to, after substituting in Eq. (1),

$$c_2(k) = Q_2(z^{-1}) \left\{ z^{-m_2} \hat{P}_2^{-1}(z^{-1}) [P_1(z^{-1}) - \hat{P}_1(z^{-1})] u_1(k) + z^{-m_2} [\hat{P}_2^{-1}(z^{-1})P_2(z^{-1}) - 1] u_2(k) + z^{-m_2} \hat{P}_2^{-1}(z^{-1}) d(k) \right\}. \quad (4)$$

If $P_i(z^{-1}) = \hat{P}_i(z^{-1})$, Eq. (4) reduces to

$$c_2(k) = Q_2(z^{-1}) z^{-m_2} \hat{P}_2^{-1}(z^{-1}) d(k). \quad (5)$$

Recall in Fig. 2, that

$$y(k) = P_1(z^{-1})u_1(k) + P_2(z^{-1})u_2^*(k) + (d(k) - P_2(z^{-1})c_2(k))$$

where $u_1(k)$ and $u_2^*(k)$ are from the outer-loop controller and $d(k) - P_2(z^{-1})c_2(k)$ explains how the external disturbance is compensated in the inner DDOB loop. Applying Eq. (5), we have

$$d(k) - P_2(z^{-1})c_2(k) = (1 - z^{-m_2}Q_2(z^{-1}))d(k). \quad (6)$$

Equation (6) contains no information about the first controlled channel. It is now seen that the disturbance rejection is entirely decoupled to the second channel, and relies on the design of a single filter $Q_2(z^{-1})$. By the above construction, $d(k)$ is decoupled from $y_1(k)$, the position output of the first actuator, and "observed" in the compensation signal $c_2(k)$.

Remark: Consider a special case where $d(k) = P_2(z^{-1})d_2(k)$ in Eq. (2), namely, disturbances occur only at the input of $P_2(z^{-1})$. The left hand side of Eq. (6) then becomes $P_2(z^{-1})[d_2(k) - c_2(k)]$. It is thus seen that $c_2(k)$ is an approximation of the equivalent input disturbance for the second actuator.

3.2 Model-following Property

In the case when $P_i(z^{-1}) \neq \hat{P}_i(z^{-1})$, the model mismatch is actually treated as an internal disturbance in the controller structure. To see this, recall the construction of the compensation signal in Eqs. (4) and (5). When $P_i(z^{-1}) \neq \hat{P}_i(z^{-1})$, Eq. (4) contains the actual disturbance effect $z^{-m_2}\hat{P}_2^{-1}(z^{-1})d(k)$ and the additional term

$$z^{-m_2} \hat{P}_2^{-1}(z^{-1}) [P_1(z^{-1}) - \hat{P}_1(z^{-1})] u_1(k) + z^{-m_2} [\hat{P}_2^{-1}(z^{-1})P_2(z^{-1}) - 1] u_2(k)$$

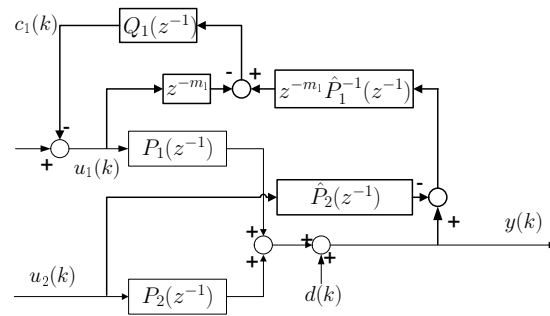
which is the equivalent internal disturbance from model mismatch.

To further analyze the absorption of the modeling errors within the DDOB loop, we derive next the dynamic relationships between $y(k)$, $d(k)$, $u_1(k)$ and $u_2^*(k)$ in Fig. 2. Notice that $c_2(k) = u_2(k) - u_2^*(k)$. Solving for $u_2(k)$ in Eq. (4) and substituting the result to Eq. (1), we can obtain the input-output relation:

$$y(k) = G_{yd}(z^{-1})d(k) + G_{yu_1}(z^{-1})u_1(k) + G_{yu_2^*}(z^{-1})u_2^*(k),$$

$$\begin{aligned} G_{yd}(z^{-1}) &= 1 - \frac{\hat{P}_2^{-1}(z^{-1})P_2(z^{-1})z^{-m_2}Q_2(z^{-1})}{1 + [\hat{P}_2^{-1}(z^{-1})P_2(z^{-1}) - 1]z^{-m_2}Q_2(z^{-1})} \\ G_{yu_1}(z^{-1}) &= P_1(z^{-1}) - \frac{\hat{P}_2^{-1}(z^{-1})P_2(z^{-1})[P_1(z^{-1}) - \hat{P}_1(z^{-1})]z^{-m_2}Q_2(z^{-1})}{1 + [\hat{P}_2^{-1}(z^{-1})P_2(z^{-1}) - 1]z^{-m_2}Q_2(z^{-1})} \\ G_{yu_2}^*(z^{-1}) &= \frac{P_2(z^{-1})}{1 + [\hat{P}_2^{-1}(z^{-1})P_2(z^{-1}) - 1]z^{-m_2}Q_2(z^{-1})}. \end{aligned}$$

One can remark that if a single DDOB already achieves canceling the disturbance, say, $d(k) - P_1(z^{-1})c_1(k)$ approximates 0, then the second DDOB is not necessary



We propose to apply frequency-dependent DDOBs based on the actuator dynamics and disturbance properties. For example, in HDD applications, recall that the VCM actuator $P_1(z^{-1})$ has a large actuation range and the microactuator $P_2(z^{-1})$ suits only for small-range positioning. Additionally, $\hat{P}_1^{-1}(z^{-1})$ has properties similar to a double differentiator [2, 18], yielding large high-frequency noises in the output of $\hat{P}_1^{-1}(z^{-1})$. Such actuator dynamics renders DDOB for VCM to have increased difficulties at high frequencies. The microactuator on the other hand has a model of a DC gain plus resonances above 4 kHz, and hence a better signal-to-noise ratio during implementation of $\hat{P}_2^{-1}(z^{-1})$. From the above considerations, in the low-frequency region, we can apply DDOB to the large-stroke VCM actuator, by assigning $Q_1(z^{-1})$ to be a low-pass/band-pass filter and $Q_2(e^{-j\omega}) \approx 0$. At middle and high frequencies, the precise and faster-response microactuator can be more effectively used. This is achieved by assigning $Q_1(e^{-j\omega}) \approx 0$ and $Q_2(z^{-1})$ to have a band-pass structure. The above analysis applies also to general DISO systems. Throughout this paper, unless otherwise stated, we assume the above decoupled disturbance-rejection scheme.

3.4 Extension to General MISO Systems

In the construction of DDOB in Figs. 2 and 3, the function of the $\hat{P}_i(z^{-1})$ block is to remove the coupling of $u_i(k)$ in $y(k)$. Extending this concept to a general multi-input single-output system, we obtain Fig. 4, the block diagram of DDOB design for the n -th actuation stage. Here two paths are constructed for each control signal $u_i(k)$, $i = 1, \dots, n-1$: the first one through the physical actuator dynamics $P_i(z^{-1})$, and the second through the model $\hat{P}_i(z^{-1})$. Notice the minus sign after each $\hat{P}_i(z^{-1})$ block. The effect of $u_i(k)$ is thus removed from $y(k)$, and $d(k)$ is the only remaining signal component that flows into the block $z^{-m_n} \hat{P}_n^{-1}(z^{-1})$. Using analogous analysis as that in Section 3.1, we can get

$$d(k) - P_n(z^{-1})c_n(k) = (1 - z^{-m_n}Q_n(z^{-1}))d(k) \quad (9)$$

if $P_i(z^{-1}) = \hat{P}_i(z^{-1})$. Equation (9) has the same structure as Eq. (6). The same design techniques can hence be applied to the design of $Q_n(z^{-1})$.

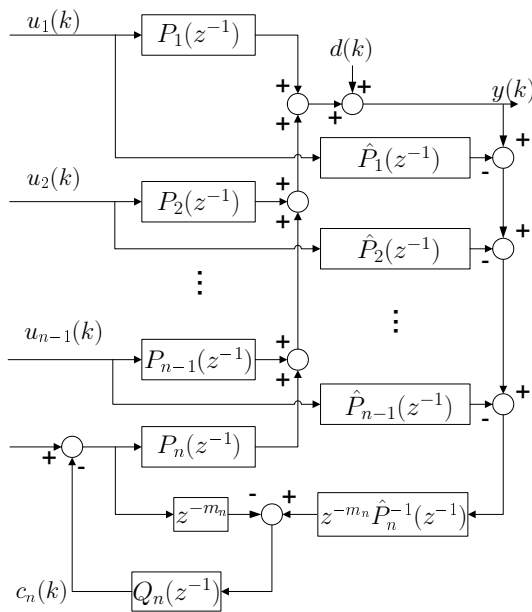


Fig. 4: DDOB for general MISO systems

4 Nominal Stability and Loop-shaping Criteria

This section discusses the design criteria and the nominal stability when DDOB is applied to a closed loop consisting of the DISO plant and a baseline feedback controller $C(z^{-1}) = [C_1(z^{-1}), C_2(z^{-1})]^T$. Fig. 5 shows the proposed controller implementation. We focus on the regulation problem to reject $d(k)$, and assume r is zero for stability and loop-shaping analysis. We will present analysis of DDOB for the secondary actuator.

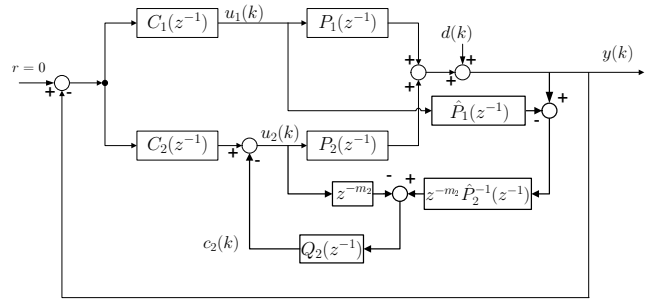


Fig. 5: Closed-loop structure with DDOB for $P_2(z^{-1})$

The result for the first actuator is immediate after interchanging the sub-indexes in the transfer functions.

For simplified analysis, the influence of DDOB can be absorbed into the second-channel controller:

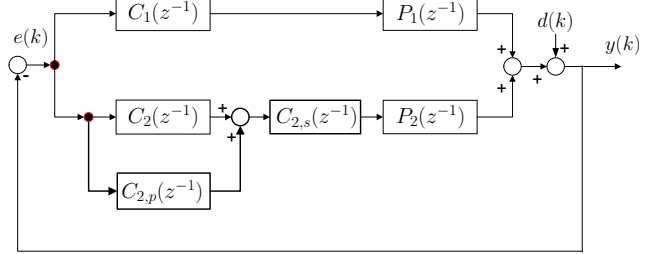


Fig. 6: An equivalent form of the system in Fig. 5

Proposition 1. The block diagram in Fig. 5 is equivalent to the one in Fig. 6, with

$$C_{2,s}(z^{-1}) = \frac{1}{1 - z^{-m_2}Q_2(z^{-1})} \quad (10)$$

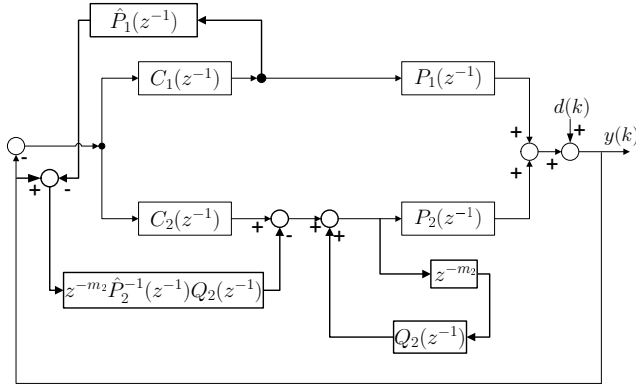
$$C_{2,p}(z^{-1}) = [1 + \hat{P}_1(z^{-1})C_1(z^{-1})]z^{-m_2}\hat{P}_2^{-1}(z^{-1})Q_2(z^{-1}). \quad (11)$$

Remark: No assumptions have been made about the perfect-model condition here. Proposition 1 holds regardless of whether $P_i(z^{-1}) = \hat{P}_i(z^{-1})$ or not.

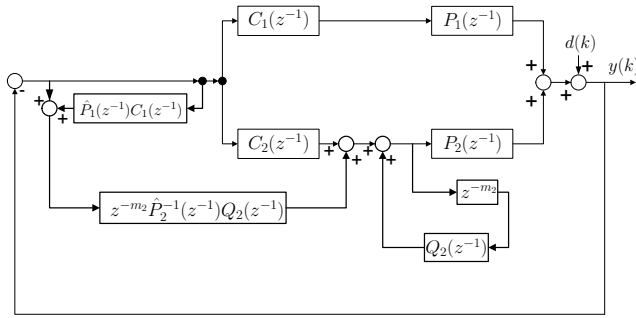
Proof. Splitting the output of $Q_2(z^{-1})$ into two parts, and relocating the summing junction after $\hat{P}_1(z^{-1})$, we get Fig. 7a. Since the reference is zero, Fig. 7a is equivalent to Fig. 7b.

Finally noting that the $\hat{P}_1(z^{-1})C_1(z^{-1})$ block in Fig. 7b does not influence the path from $C_1(z^{-1})$ to $P_1(z^{-1})$, we obtain Fig. 8a, which is equivalent to Figs. 8b and 6, with the add-on serial and parallel terms given by Eq. (10) and Eq. (11). ■

From Fig. 6 and Proposition 1, the open-loop trans-

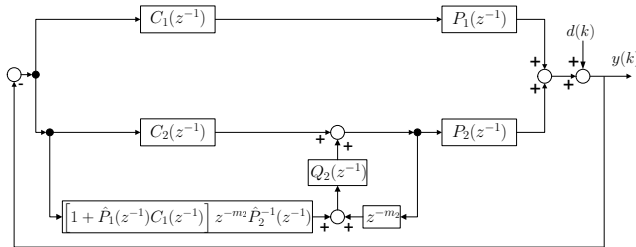


(a) An equivalent block diagram of the system in Fig. 5: the input to $z^{-m_2} \hat{P}_2^{-1}(z^{-1})$ is relocated; the summing junction before $Q_2(z^{-1})$ is separated

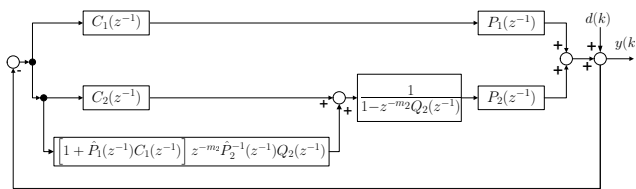


(b) An equivalent block diagram of the system in Fig. 7a: the signs of the signals are changed after another relocation of block diagrams

Fig. 7: Block diagram transformation for Fig. 5



(a) An equivalent form of Fig. 7b



(b) An equivalent form of Fig. 8a

Fig. 8: Block diagram transformation for Fig. 7: DDOB is decomposed to series and parallel modules

fer function from the error $e(k)$ to the output $y(k)$ is¹

$$L = P_1 C_1 + P_2 C_{2,s} (C_2 + C_{2,p}) \quad (12)$$

$$= P_1 C_1 + P_2 \frac{C_2 + (1 + \hat{P}_1 C_1) z^{-m_2} \hat{P}_2^{-1} Q_2}{1 - z^{-m_2} Q_2}. \quad (13)$$

If $P_i = \hat{P}_i$, Eq. (13) simplifies to

$$L = \frac{P_1 C_1 + P_2 C_2 + z^{-m_2} Q_2}{1 - z^{-m_2} Q_2}.$$

The sensitivity function of the closed-loop system, namely, the transfer function from the output disturbance $d(k)$ to $y(k)$, is therefore given by

$$S = G_{yd} = \frac{1}{1+L} = \frac{1 - z^{-m_2} Q_2}{1 + P_1 C_1 + P_2 C_2}. \quad (14)$$

Notice that $1/(1 + P_1 C_1 + P_2 C_2)$ is the *stable* baseline closed-loop sensitivity function if $C_{2,s}(z^{-1}) = 1$ and $C_{2,p}(z^{-1}) = 0$. One can observe that S therefore is stable as long as Q_2 is stable. This is quite beneficial for flexible servo design, as the stability condition can be easily satisfied. In addition, $1 - z^{-m_2} Q_2$ can be applied as a frequency-domain design criteria for the desired loop shaping. In the frequency regions where $z^{-m_2} Q_2|_{z=e^{j\omega}}$ is approximately 1, $S \approx 0$, i.e., the closed-loop system has enhanced disturbance rejection. When $z^{-m_2} Q_2|_{z=e^{j\omega}}$ is approximately 0, S is close to its baseline version and the original system response is preserved.

With slightly more algebra, we can obtain the closed-loop internal stability condition:

Theorem 1. (nominal stability) *Given an internally stable baseline feedback system in Fig. 5, if $P_i(z^{-1}) = \hat{P}_i(z^{-1})$, and $\hat{P}_2^{-1}(z^{-1})$ is stable, then the closed-loop system in Fig. 5 is internally stable as long as $Q_2(z^{-1})$ is stable.*

Proof. See Appendix A.

5 Robust Stability

Since plant uncertainty always exists in reality, the actual implementation of the Q filter needs to consider the robust stability condition. This section analyzes the situation when the actual plant differs from the nominal model by:

$$P_1(e^{-j\omega}) = \hat{P}_1(e^{-j\omega}) (1 + W_1(e^{-j\omega}) \Delta_1(e^{-j\omega})) \quad (15)$$

$$P_2(e^{-j\omega}) = \hat{P}_2(e^{-j\omega}) (1 + W_2(e^{-j\omega}) \Delta_2(e^{-j\omega})), \quad (16)$$

where $W_1(e^{-j\omega})$ and $W_2(e^{-j\omega})$ are weighting functions and the perturbations satisfy $|\Delta_i(e^{-j\omega})| \leq 1$. We assume that the perturbations do not alter stability of the system, i.e., W_i and Δ_i are stable.

Since the DISO system is a special MIMO system, the μ -analysis (see, e.g., [19]) tool can naturally be applied to derive the robust stability condition. Usually, the structured singular value μ is only approximated by its upper bound. However, for the special case of DISO plants, we have a closed-form solution for μ , as described in the following theorem.

¹For the sake of brevity, the index (z^{-1}) is omitted here. This simplification of notation will be adopted for long equations in the remainder of the paper.

Theorem 2. *The closed-loop system in Fig. 5 is stable w.r.t. the perturbed plant in Eq. (15) and Eq. (16), if and only if nominal stability holds and the following structured singular value satisfies $\mu < 1$:*

$$\mu = \frac{|1 - z^{-m_2} Q_2| |\hat{P}_1 C_1| |W_1|}{|1 + \hat{P}_1 C_1 + \hat{P}_2 C_2|} + \frac{|\hat{P}_2 C_2 + (1 + \hat{P}_1 C_1) z^{-m_2} Q_2| |W_2|}{|1 + \hat{P}_1 C_1 + \hat{P}_2 C_2|}. \quad (17)$$

Proof. See Appendix B.

Notice that μ is linear w.r.t. $|W_1|$ and $|W_2|$. Overall Eq. (17) indicates that in the regions where a good model is available for the plant ($|W_1|$ and $|W_2|$ are small), the structured singular value is small and we have flexible design freedom in $Q_2(z^{-1})$. If $e^{-m_2 j \omega} Q_2(e^{-j \omega}) = 0$, DDOB is turned off at this frequency and Eq. (17) is simply the structured singular value of the baseline feedback system. This infers that the baseline system needs to be robustly stable. In the frequency region where $e^{-m_2 j \omega} Q_2(e^{-j \omega})$ is close to unity, $\mu \approx |W_2|$, namely, the robust stability depends on the magnitude of model uncertainty of the secondary actuator. Therefore, if $|W_2|$ goes beyond 1 at certain frequencies (particularly true when approaching the Nyquist frequency), certainly one should not apply the model-based DDOB here, and the magnitude of $Q(z^{-1})$ should be kept small. For dual-stage HDDs, accuracy of the model is usually preserved up to at least 5kHz, providing a large frequency range for flexible Q-filter design to satisfy $\mu < 1$.

6 Optimal Q-filter Design

From Eq. (14), forming $Q(z^{-1})$ as a low-pass filter yields the enhanced low-frequency servo performance that is similar to conventional SISO DOBs [1]. Various researches have been conducted to design such Q filters [12–14]. For vibration rejection, the disturbance is not restricted to occur at low frequencies. In this case, it is more beneficial to assign a band-pass property to $Q(z^{-1})$. This section provides an optimal design of $Q(z^{-1})$ for loop shaping at selective frequency locations. By using convex optimization techniques, we are able to design $Q(z^{-1})$ with arbitrary magnitude (upper) bounds, and at the same time minimize the disturbance amplification (coming from the waterbed effect in the fundamental limitations of feedback design) in the closed-loop system.

Consider the following construction for Eq. (14):

$$1 - z^{-m} Q(z^{-1}) = F_{nf}(z^{-1}) K(z^{-1}) \quad (18)$$

$$K(z^{-1}) = k_1 + k_2 z^{-1} + \dots + k_{n_k+1} z^{-n_k}, \quad (19)$$

where $z^{-m} Q(z^{-1})$ can be either $z^{-m_1} Q_1(z^{-1})$ or

$z^{-m_2} Q_2(z^{-1})$; $F_{nf}(z^{-1})$ is a filter that provides the desired low gains (in a range of frequencies) to Eq. (14); and $K(z^{-1})$ a n_k -order finite-impulse-response (FIR) filter that is introduced for realizability of $Q(z^{-1})$ and for providing additional optimal properties to $Q(z^{-1})$.

Although our analysis is valid for general choice of filter in $F_{nf}(z^{-1})$, we will focus on vibration rejection and provide design details for the case when $F_{nf}(z^{-1})$ is a notch filter.

6.1 Causality of $Q(z^{-1})$

Let

$$F_{nf}(z^{-1}) = \frac{B_{nf}(z^{-1})}{A_{nf}(z^{-1})}$$

with $B_{nf}(z^{-1}) = b_1 + b_2 z^{-1} + \dots + b_{n_b+1} z^{-n_b}$ and $A_{nf}(z^{-1}) = a_1 + a_2 z^{-1} + \dots + a_{n_a+1} z^{-n_a}$. Solving Eq. (18) gives

$$Q(z^{-1}) = z^m \frac{A_{nf}(z^{-1}) - B_{nf}(z^{-1}) K(z^{-1})}{A_{nf}(z^{-1})} =: z^m \frac{X(z^{-1})}{A_{nf}(z^{-1})}. \quad (20)$$

Expanding the convolution $B_{nf}(z^{-1}) K(z^{-1})$ and grouping the coefficients in $A_{nf}(z^{-1}) - B_{nf}(z^{-1}) K(z^{-1})$, we obtain

$$X(z^{-1}) = (a_1 - b_1 k_1) + (a_2 - b_2 k_1 - b_1 k_2) z^{-1} + \dots + \left(a_i - \sum_{j=0}^{i-1} b_{i-j} k_{j+1} \right) z^{-i+1} + \dots \quad (21)$$

Since z^m is not causal $\forall m > 0$, to have a realizable $Q(z^{-1})$ in Eq. (20), the coefficients of z^{-i} need to be zero for $i = 0, 1, \dots, m-1$ in $X(z^{-1})$, namely, [by writing the coefficients of Eq. (21) in vector product form]

$$\underbrace{\begin{bmatrix} a_1 \\ a_2 \\ \vdots \\ a_m \end{bmatrix}}_{\tilde{A}} - \underbrace{\begin{bmatrix} b_1 & 0 & \dots & 0 & 0_{1,n_k+1-m} \\ b_2 & b_1 & 0 & \vdots & 0_{1,n_k+1-m} \\ \vdots & \ddots & \ddots & 0 & 0_{1,n_k+1-m} \\ b_m & \dots & b_2 & b_1 & 0_{1,n_k+1-m} \end{bmatrix}}_{\tilde{B}} \begin{bmatrix} k_1 \\ k_2 \\ \vdots \\ k_{n_k+1} \end{bmatrix} = \begin{bmatrix} 0 \\ 0 \\ \vdots \\ 0 \end{bmatrix}. \quad (22)$$

Here $a_i = 0$ if $i > n_a$ and $b_i = 0$ if $i > n_b$. Notice the columns of \tilde{B} span \mathbb{R}^m if $b_1 \neq 0$. Therefore, $n_k + 1$ has to be no smaller than m for a solution to exist for a general $\tilde{A} \in \mathbb{R}^m$, i.e., 1 plus the order of $K(z^{-1})$ has to be no smaller than the number of plant delays.

As an example, if $m = 4$

$$F_{nf}(z^{-1}) = \frac{1 - 2\beta \cos \omega_0 z^{-1} + \beta^2 z^{-2}}{1 - 2\alpha \cos \omega_0 z^{-1} + \alpha^2 z^{-2}}$$

and $n_k = 3$, Eq. (22) reduces to

$$\begin{bmatrix} 1 \\ -2\alpha \cos \omega_0 \\ \alpha^2 \\ 0 \end{bmatrix} - \begin{bmatrix} 1 & 0 & 0 & 0 \\ -2\beta \cos \omega_0 & 1 & 0 & 0 \\ \beta^2 & -2\beta \cos \omega_0 & 1 & 0 \\ 0 & \beta^2 & -2\beta \cos \omega_0 & 1 \end{bmatrix} \begin{bmatrix} k_1 \\ k_2 \\ k_3 \\ k_4 \end{bmatrix} = \begin{bmatrix} 0 \\ 0 \\ 0 \\ 0 \end{bmatrix} \quad (23)$$

Solving the above equation for k_i and substituting the results to Eq. (20), we obtain

$$Q(z^{-1}) = \frac{-\beta^2 k_3 + 2\beta \cos \omega_0 k_4 - \beta^2 k_4 z^{-1}}{1 - 2\alpha \cos \omega_0 z^{-1} + \alpha^2 z^{-2}} \quad (24)$$

where $k_3 = \alpha^2 - \beta^2 + 2\beta \cos \omega_0 k_2$, $k_4 = -\beta^2 k_2 + 2\beta \cos \omega_0 k_3$, $k_2 = -2\cos \omega_0 (\alpha - \beta)$, and $k_1 = 1$.

6.2 Optimal Performance

As can be seen in the last section, if $n_k + 1 = m$, the m equations in Eq. (22) define a unique solution for $K(z^{-1})$. Additionally, n_k can be set to be larger than $m - 1$ to allow more design freedom in $Q(z^{-1})$. First, recalling Eq. (14), we can minimize the infinity norm of $1 - z^{-m}Q(z^{-1})$ (maximum magnitude of $|1 - e^{-jm\omega}Q(e^{-j\omega})|$), which will in turn minimize the disturbance amplification in the sensitivity function. This can be achieved by minimizing $\|K(z^{-1})\|_\infty$ in Eq. (18). Second, as discussed in Section 5, to keep the system robustly stable, the magnitude of $Q(z^{-1})$ should be small at frequencies outside its passband, especially where large model uncertainty exists (normally in the high-frequency region). These two objectives can be formulated into the following optimization problem:

Find k_1, \dots, k_{n_k+1} to

$$\text{minimize: } J = \|K(z^{-1})\|_\infty \quad (25)$$

$$\text{subject to: } \tilde{A} - \tilde{B} [k_1, \dots, k_{n_k+1}]^T = 0 \quad (26)$$

$$|Q(e^{-j\omega})| \leq \delta(\omega), \quad \omega = \omega_1, \omega_2, \dots \quad (27)$$

where \tilde{A} and \tilde{B} are as defined in Eq. (22); and $\delta(\omega)$ is the user-defined magnitude upper bound at frequency ω (in rad).

The causality constraint Eq. (26) is a set of linear equations (explicitly $n_k > m - 1$ is assumed in this case). Equation (25) and Eq. (27) however are nonlinear and not yet convex.

For the H_∞ performance objective, the bounded-real lemma can translate Eq. (25) to a linear matrix inequality (LMI).

Lemma 1: (Bounded-real lemma; see, e.g., [20, 21]) Let (A, B, C, D) be the state-space realization of a stable and controllable discrete-time system G . Then for a positive number γ , $\|G\|_\infty \leq \gamma$ if and only if there exists a symmetric matrix M such that

$$\begin{bmatrix} A^T M A - M & A^T M B & C^T \\ B^T M A & B^T M B - \gamma I & D^T \\ C & D & -\gamma I \end{bmatrix} \leq 0, \quad M > 0.$$

For the magnitude constraints in Eq. (27), after some complex analysis, we can transform it to a set of convex quadratic constraints. To do so, notice first, that

$$Q(z^{-1}) = z^m (1 - F_{nf}(z^{-1})K(z^{-1})). \quad (28)$$

Constraining $|Q(e^{-j\omega})| \leq \delta(\omega)$ is equivalent to requiring $|Q(e^{-j\omega})|^2 \leq \delta^2(\omega)$. The z^m term has unity gain $\forall z = e^{j\omega}$, and can be dropped in the magnitude design. The frequency response of $K(e^{-j\omega})$ is

$$K(e^{-j\omega}) = \sum_{n=1}^{n_k+1} k_n e^{-j\omega(n-1)} = \phi_r^T(\omega)\theta - j\phi_i^T(\omega)\theta \quad (29)$$

where

$$\begin{aligned} \phi_r^T(\omega) &= [1 \cos(\omega) \dots \cos(n_k \omega)] \\ \phi_i^T(\omega) &= [0 \sin(\omega) \dots \sin(n_k \omega)] \\ \theta^T &= [k_1 \ k_2 \ \dots \ k_{n_k+1}]. \end{aligned}$$

Let $F_{nf}(e^{-j\omega}) = F_r(\omega) - jF_i(\omega)$. Then Eq. (29) gives $F_{nf}(e^{-j\omega})K(e^{-j\omega}) = \psi_r^T(\omega)\theta - j\psi_i^T(\omega)\theta$, where $\psi_r^T(\omega) = F_r(\omega)\phi_r^T(\omega) - F_i(\omega)\phi_i^T(\omega)$ and $\psi_i^T(\omega) = F_r(\omega)\phi_i^T(\omega) + F_i(\omega)\phi_r^T(\omega)$. Hence

$$1 - F_{nf}(e^{-j\omega})K(e^{-j\omega}) = 1 - \psi_r^T(\omega)\theta + j\psi_i^T(\omega)\theta.$$

By computing

$$\begin{aligned} &|1 - F_{nf}(e^{-j\omega})K(e^{-j\omega})|^2 \\ &= \overline{(1 - F_{nf}(e^{-j\omega})K(e^{-j\omega}))} (1 - F_{nf}(e^{-j\omega})K(e^{-j\omega})) \end{aligned}$$

we finally obtain the following quadratic constraint

$$\begin{aligned} |Q(e^{-j\omega})|^2 &= \theta^T [\psi_r(\omega)\psi_r^T(\omega) + \psi_i(\omega)\psi_i^T(\omega)]\theta \\ &\quad - 2\psi_r^T(\omega)\theta + 1 \leq \delta^2(\omega). \end{aligned}$$

Notice that $\psi_r(\omega)\psi_r^T(\omega) + \psi_i(\omega)\psi_i^T(\omega)$ is positive semi-definite. The above constraint is thus convex in θ .

Summarizing the above discussions, we obtain the following explicit form of Eqs. (25)-(27)

$$\min_{\theta, M, \gamma} : \gamma \quad (30)$$

$$\text{subject to: } \tilde{B}\theta = \tilde{A}$$

$$\begin{bmatrix} A^T M A - M & A^T M B & C^T \\ B^T M A & B^T M B - \gamma I & D^T \\ C & D & -\gamma I \end{bmatrix} \leq 0 \quad (31)$$

$$M > 0, \gamma > 0 \quad (32)$$

$$\theta^T [\psi_r(\omega)\psi_r^T(\omega) + \psi_i(\omega)\psi_i^T(\omega)] \theta \quad (33)$$

$$-2\psi_r^T(\omega)\theta + 1 \leq \delta^2(\omega), \omega = \omega_1, \omega_2, \dots$$

Here Eq. (30) represents “minimize γ with respect to the variables θ, M , and γ ”. We have translated the objective of minimizing $\|K(z^{-1})\|_\infty$ in Eq. (25) to minimizing γ , subject to Eq. (31) and Eq. (32), by applying Lemma 1. In Eq. (31), A, B, C and D are the state-space matrices of $K(z^{-1})$. To make Eq. (31) linear in the decision variables θ and M , we choose the controllable canonical form of Eq. (19):

$$A = \begin{bmatrix} 0_{n_k-1,1} & I_{n_k-1} \\ 0 & 0_{1,n_k-1} \end{bmatrix}, B = \begin{bmatrix} 0_{n_k-1,1} \\ 1 \end{bmatrix}$$

$$C = [k_2, \dots, k_{n_k+1}], D = k_1.$$

The entire optimization problem is now convex, and can be efficiently solved using the interior-point method (see, e.g., [22]) in mathematical optimization.

6.3 Optimization Result

As an example, let $m = 2$ and $F_{nf}(z^{-1}) = \frac{1-2\beta\cos\omega_0 z^{-1} + \beta^2 z^{-2}}{1-2\alpha\cos\omega_0 z^{-1} + \alpha^2 z^{-2}}$, where $\omega_0 = 2\pi\Omega_{Hz}T_s$ (Ω_{Hz} is the center frequency in Hz, T_s is the sampling time in sec); α is related to the -3dB bandwidth (denoted as BW in radian) by the relationship $\alpha \approx \sqrt{\frac{1-\tan(BW/2)}{1+\tan(BW/2)}}$. Since $m = 2$, the order of $K(z^{-1})$ should be no smaller than one here. Consider the case of $\Omega_{Hz} = 2000$, $T_s = 0.04$ ms, $BW = 2\pi T_s \times 500$ rad, and $\beta = 0.999$. Fig. 9 demonstrates the magnitude responses of $Q(z^{-1})$ and $1 - z^{-m}Q(z^{-1})$ using the proposed algorithms. Also plotted are the results if we ignore z^{-m} and directly assign a standard band-pass filter $Q(z^{-1}) = 1 - F_{nf}(z^{-1})$ in Eq. (18).

Notice first, from the second plot, that a standard band-pass filter does not create the desired magnitude response in $1 - z^{-m}Q(z^{-1})$. A notch was introduced at the wrong frequencies, and there are undesired large gains at around 2100 Hz. On the contrary, the causal and optimal designs correctly introduce a sharp notch at the desired frequency. Second, compared to the

causal solution, the optimal solution enforces reduced gains in $Q(z^{-1})$. In this example, the magnitude of $Q(z^{-1})$ is constrained to be no larger than -40dB at $\{0, 6000, 7500, 10000, 12500$ (Nyquist frequency)) Hz. Besides the enhanced robust stability in the high-frequency region, constraining the gains of $Q(z^{-1})$ also keeps the magnitude of $1 - z^{-m}Q(z^{-1})$ closer to unity (better preservation of the baseline loop shape). As a trade off, compared to the causal solution, the magnitude of $1 - z^{-m}Q(z^{-1})$ is slightly increased around 3000 Hz. In practice, if the causal solution already provides robust stability and the desired loop shape, one can directly use the result of Eq. (22) for $Q(z^{-1})$.

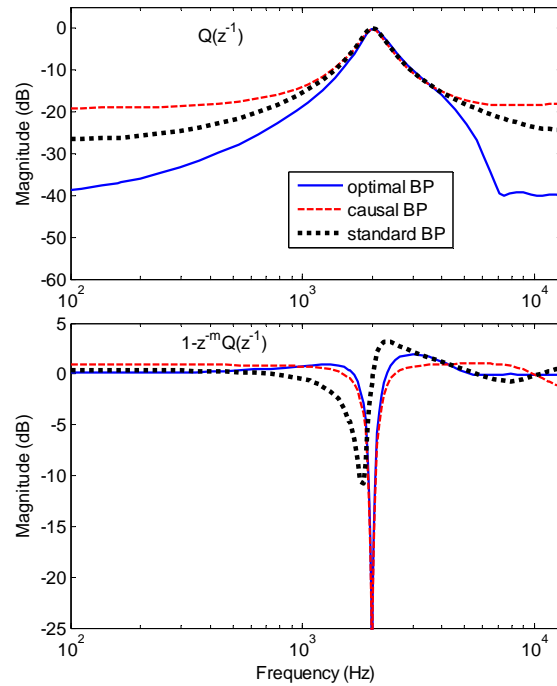


Fig. 9: Q design example: BP denotes band-pass filter; the standard BP equals $1 - F_{nf}(z^{-1})$; the causal BP is from Section 6.1; and the optimal BP comes from Eq. (25)-(27)

Remark: For the case where multiple bands are desired in the notch filter, $F_{nf}(z^{-1})$ can be modified to, e.g.

$$F_{nf}(z^{-1}) = \prod_{i=1}^{n_{nf}} \frac{1 - 2\beta_i z^{-1} \cos \omega_i + \beta_i^2 z^{-2}}{1 - 2\alpha_i z^{-1} \cos \omega_i + \alpha_i^2 z^{-2}}$$

where n_{nf} is the number of bands in the notch shape, $1 > \beta_i > 0$ (α_i, β_i close to one), and the unit of ω_i is radian.

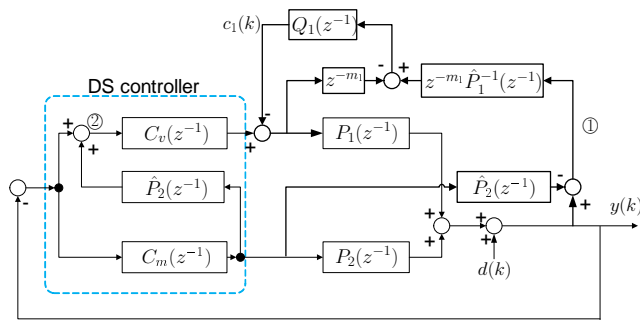


Fig. 10: Block diagram of the closed-loop system with DDOB and decoupled sensitivity control

7 Decoupled Sensitivity and DDOB

This section discuss a reduced-order implementation of DDOB for the the first actuator in DISO systems. The main result is that, DDOB provides a natural enhancement scheme to the decoupled sensitivity (DS) feedback design, which is the most popular design technique in dual-stage HDDs (see, e.g., [23–25]).

In Fig. 10, the DS controller has the transfer function $C(z^{-1}) = [C_v(z^{-1})(1 + \hat{P}_2(z^{-1})C_m(z^{-1})), C_m(z^{-1})]^T$ (the sub-indexes v and m represent VCM and microactuator respectively). Consider first the baseline system formed only by $P_1(z^{-1})$, $P_2(z^{-1})$ and $C(z^{-1})$. The idea of decoupled sensitivity design is that, if $P_2(z^{-1}) = \hat{P}_2(z^{-1})$, direct computation gives

$$1 + P(z^{-1})C(z^{-1}) = (1 + P_1(z^{-1})C_v(z^{-1}))(1 + P_2(z^{-1})C_m(z^{-1})).$$

Consequently, the total sensitivity function $S(z^{-1}) = 1/(1 + P(z^{-1})C(z^{-1}))$ is decoupled to the cascaded connection of $1/(1 + P_1(z^{-1})C_v(z^{-1}))$ and $1/(1 + P_2(z^{-1})C_m(z^{-1}))$.

Consider the combined implementation of DS and DDOB for the first actuator in Fig. 10. Notice that $\hat{P}_2(z^{-1})$ appears in both DDOB and the DS controller. In addition, since the reference is zero in regulation control, the signals at ① and ② can be seen to be negatives of each other. We can thus replace the input of $z^{-m_1}\hat{P}_1^{-1}(z^{-1})$ by the negative of the signal at ②. With some block-diagram relocation and sign rearrangement, we obtain Fig. 11, the equivalent realization of the block diagram in Fig. 10. Notice that we have now saved the computation of one $\hat{P}_2(z^{-1})$ block. Fig. 11 is simpler to implement and analyze as well.

8 Case Study

The effectiveness of the DDOB design has been successfully evaluated by both a HDD benchmark simulation tool and experiments on an industrial test drive HDD. We present first detailed evaluation results for the simulated benchmark that uses the system configuration on page 195 of the book [26]. The plant

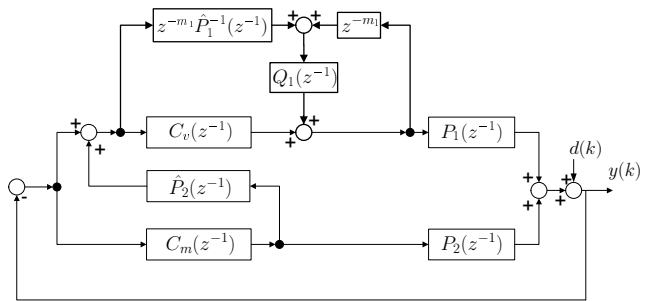


Fig. 11: A reduced-order implementation of Fig. 10

model comes from identification of an actual experimental setup. A set of disturbance data is modified from audio-vibration tests on an actual HDD. We will design DDOBs for both the Voice-Coil-Motor (VCM) actuator and the microactuator (MA). The former is denoted as VCM DDOB, and the latter as MA DDOB.

Fig. 12 shows the frequency response of the plant. Two major resonances exist in the VCM actuator, and are compensated via two notch filters at 3.0 kHz and 6.5 kHz. The 11-order resonance-compensated VCM model is treated as a generalized plant $P_1(z^{-1})$. $P_1(z^{-1})$ is chosen to be a second-order transfer function that captures the friction mode at around 60 Hz in Fig. 12, with a 2-step delay (i.e., $m_1 = 2$). After the above construction, one non-minimum-phase zero appears in $\hat{P}_1(z^{-1})$ near the Nyquist frequency. This zero is replaced with a stable one that lies strictly inside the unit circle, yielding the final nominal model shown in Fig. 13. Through the above design, both the magnitude and the phase of $P_1(z^{-1})$ is well captured by $\hat{P}_1(z^{-1})$ up to around 6 kHz.

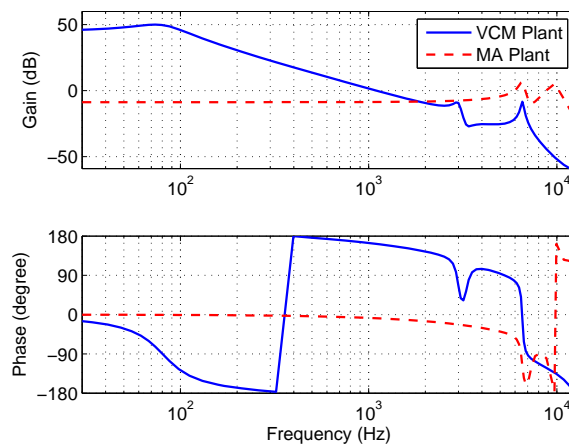
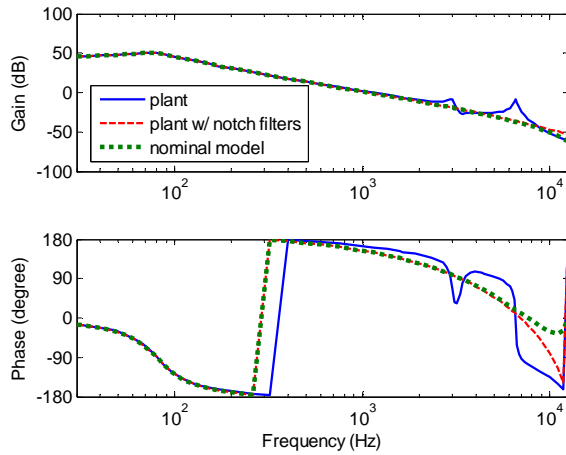


Fig. 12: Frequency responses of the plant models

The microactuator also contains two resonances that are compensated by notch filters. This actuator is a minimum-phase system by nature. We directly

Fig. 13: $\hat{P}_1(z^{-1})$ for DDOB in VCM actuator

model $\hat{P}_2(z^{-1})$ to include the resonances, with $m_2 = 1$ in the MA DDOB.

8.1 Nominal Performance

The decoupled sensitivity design is used to form the baseline feedback loop: a lead-lag compensator for the VCM stage; and a lag compensator for the MA stage. The baseline closed-loop sensitivity function has the magnitude response shown in the solid thick line in Fig. 14. One can recognize that such a loop shape is quite standard in feedback control.

VCM and MA DDOBs are configured in the forms of Fig. 11 and Fig. 5 respectively. The flexibility of the algorithm is explained in Fig. 14, where we use the same structure of $Q_i(z^{-1})$ but with different center-frequency configurations. Six Q filters are evaluated, with the resulting six sensitivity functions plotted in an overlaid fashion. The first three gain reductions come from VCM DDOB with $Q_1(z^{-1})$ centered at 500 Hz, 900 Hz, and 1500 Hz respectively. The remaining three are generated by MA DDOB [$Q_2(z^{-1})$ centered at 2300 Hz, 3100 Hz, and 3900 Hz]. It is observed that by simple alternation of Q filters, the servo loop can be customized to a great extent. Also, in HDD applications, 3900 Hz is a very high frequency for disturbance attenuation, one that is rarely seen in previous literatures.

8.2 Performance Under Plant Perturbations

A set of perturbation profiles is applied to the plant to reflect the uncertainties in the system. Fig. 15 shows the magnitude of the perturbations [$W_i\Delta_i$ in Eqs. (15) and (16)] at different frequencies. This is a very typical uncertainty set in precision control, where the plant dynamics has large variations only at high frequencies.

With the DDOB configurations in Table 1, we obtain the sensitivity functions in Fig. 16. The design is for attenuating vibrations in a later example in Fig. 18. Since

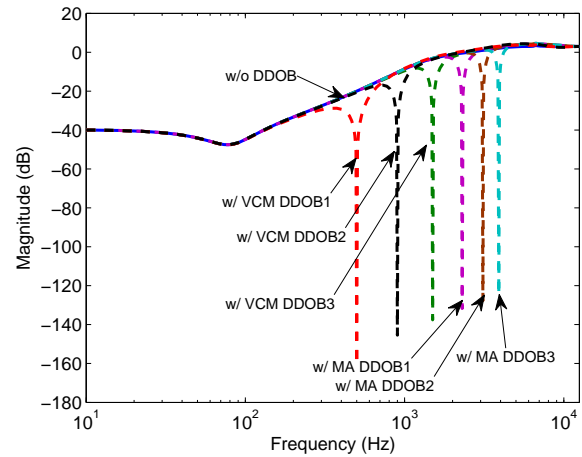


Fig. 14: Magnitude responses of the sensitivity functions with different Q-filter configurations

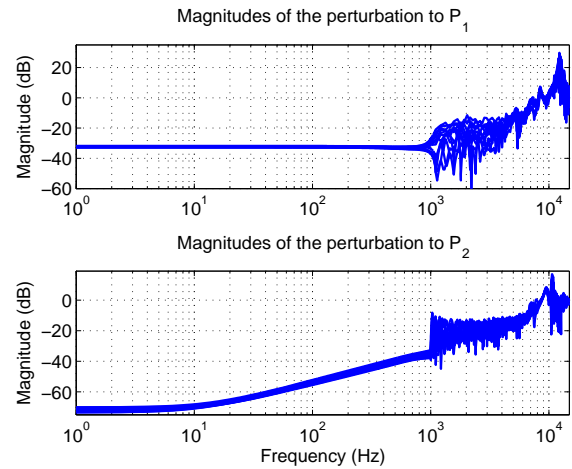


Fig. 15: Practical plant perturbations

the error peaks are non-uniform in the magnitudes, we did not make the notch shape as sharp as that in Fig. 14 (by letting $\beta < 1$ in the design of Section 6.3).

Table 1: Band-pass Q-filter Configuration in DDOBs

Actuator	Center freq.	Width of pass band	$ Q(e^{-j\omega}) $ at DC & Nyquist freq.
VCM	1200 Hz	400 Hz	$< -50\text{dB}$
MA	2900 Hz	800 Hz	$< -50\text{dB}$

It can be observed that the strong notch shapes from DDOB design were maintained under all the plant perturbations. Meanwhile, for the robust stability condition, computing the structured singular values in Fig. 17, we can confirm that the value of μ is less than one

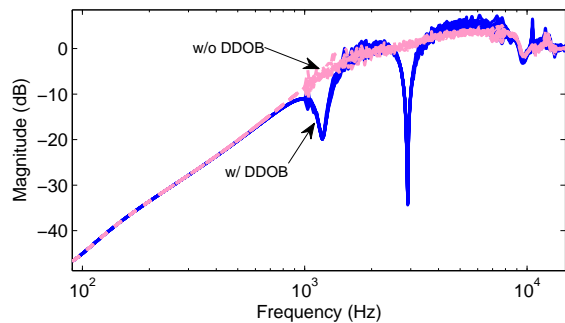


Fig. 16: Perturbed sensitivity functions with and without DDOBs

at all frequencies, indicating that the system is robustly stable. In particular, we see that the DDOB-induced servo enhancement did not create large values of μ near the center frequencies of the Q filter (1200 Hz and 2900 Hz). More critical stability constraints actually came from the large uncertainties at high frequencies.

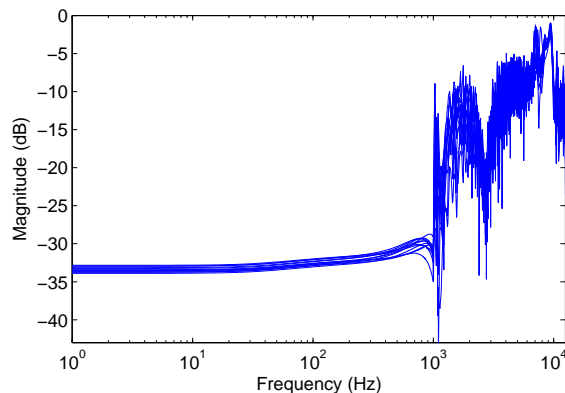


Fig. 17: Values of μ from robust-stability analysis

Figs. 18 and 19 present respectively the frequency- and time-domain audio-vibration rejection results. It can be observed that the spectral peaks at the corresponding frequencies are significantly reduced by DDOBs (recall the location of the notch shapes in Fig. 16), and in the time domain, the magnitudes of position errors are decreased by at least fifty percent compared to their original values.

For the experimental verification, two notches were introduced in the sensitivity function. Table 2 presents the performance improvements. It can be observed that in both cases, the algorithm is valid and the simulation closely matches the experimental result.

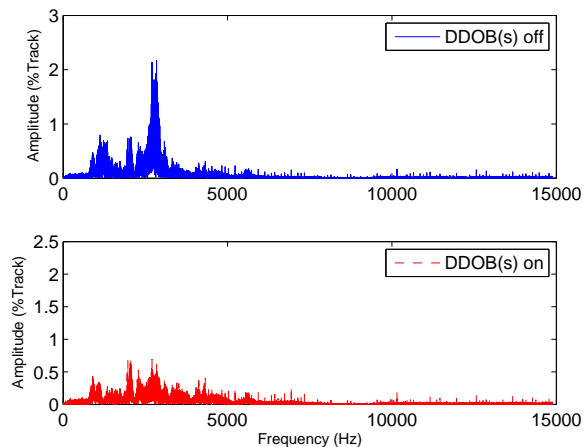


Fig. 18: Spectra of the position error signals (PES) using a projected disturbance profile

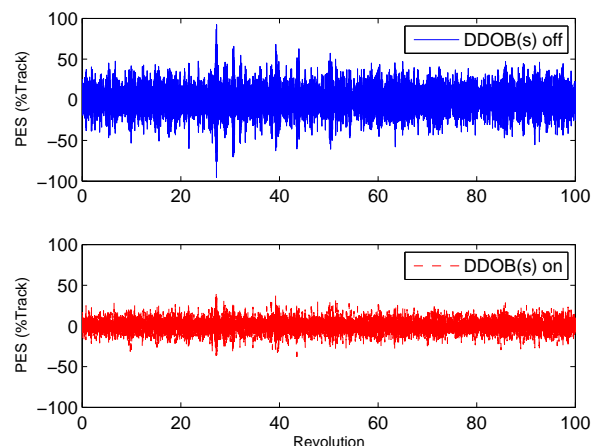


Fig. 19: Time traces of the PES signals in Fig. 18

Table 2: Magnitude reduction in sensitivity function

	simulation	experiment
notch 1	77%	75%
notch 2	86%	87%

9 Conclusions

This paper has presented a feedback control approach for servo enhancement in dual-input single-output control systems. Specifically we have discussed the application of the algorithm to compensate vibrations with wide spectral peaks in dual-stage HDDs, where the proposed algorithm provides the advantage of using the the best actuator for rejecting disturbances of different characteristics. Extension of the algorithm has also been discussed to general multi-input single-output systems. Future work includes generalization of the optimal filter design method for rejection of other

disturbances, and the application of the algorithm to other MISO systems.

Acknowledgements

This work was supported by a research grant from Western Digital Corporation, and by the Computer Mechanics Laboratory (CML) in Dept. of Mechanical Engineering, University of California, Berkeley.

References

- [1] Ohnishi, K., 1993. "Robust motion control by disturbance observer". *Journal of the Robotics Society of Japan*, **11**(4), pp. 486–493.
- [2] White, M., Tomizuka, M., and Smith, C., 2000. "Improved track following in magnetic disk drives using a disturbance observer". *IEEE/ASME Trans. Mechatronics*, **5**(1), Mar., pp. 3–11.
- [3] Chen, X., and Tomizuka, M., 2010. "Unknown multiple narrow-band disturbance rejection in hard disk drives—an adaptive notch filter and perfect disturbance observer approach". In Proc. 2010 ASME Dynamic Systems and Control Conf., pp. 936–970.
- [4] Yang, K., Choi, Y., and Chung, W. K., 2005. "On the tracking performance improvement of optical disk drive servo systems using error-based disturbance observer". *IEEE Trans. Ind. Electron.*, **52**(1), Feb., pp. 270–279.
- [5] Tan, K. K., Lee, T. H., Dou, H. F., Chin, S. J., and Zhao, S., 2003. "Precision motion control with disturbance observer for pulsewidth-modulated-driven permanent-magnet linear motors". *IEEE Trans. Magn.*, **39**(3), pp. 1813–1818.
- [6] Kempf, C. J., and Kobayashi, S., 1999. "Disturbance observer and feedforward design for a high-speed direct-drive positioning table". *IEEE Trans. Control Syst. Technol.*, **7**(5), pp. 513–526.
- [7] Eom, K. S., Suh, I. H., and Chung, W. K., 2001. "Disturbance observer based path tracking control of robot manipulator considering torque saturation". *Mechatronics*, **11**(3), pp. 325–343.
- [8] Bohn, C., Cortabarría, A. and Härtel, V., and Kowalczyk, K., 2004. "Active control of engine-induced vibrations in automotive vehicles using disturbance observer gain scheduling". *Control Engineering Practice*, **12**(8), pp. 1029–1039.
- [9] Nie, J., and Horowitz, R., 2009. "Design and implementation of dual-stage track-following control for hard disk drives". In Proc. 2nd Dynamic Systems and Control Conf., Vol. 2, pp. 565–572.
- [10] Guo, L., and Chen, W.-H., 2005. "Disturbance attenuation and rejection for systems with nonlinearity via dobc approach". *International Journal of Robust and Nonlinear Control*, **15**(3), pp. 109–125.
- [11] Zheng, Q., Chen, Z., and Gao, Z., 2009. "A practical approach to disturbance decoupling control". *Control Engineering Practice*, **17**(9), pp. 1016–1025.
- [12] Wang, C.-C., and Tomizuka, M., 2004. "Design of robustly stable disturbance observers based on closed loop consideration using h-infinity optimization and its applications to motion control systems". In Proc. 2004 American Control Conf., Vol. 4, pp. 3764–3769.
- [13] Kemp, C. C., and Kobayashi, S., 1996. "Discrete-time disturbance observer design for systems with time delay". In Proc. 1996 4th International Workshop on Advanced Motion Control, Vol. 1, pp. 332–337.
- [14] Choi, Y., Yang, K., Chung, W. K., Kim, H. R., and Suh, I. H., 2003. "On the robustness and performance of disturbance observers for second-order systems". *IEEE Trans. Autom. Control*, **48**(2), Feb., pp. 315–320.
- [15] Chen, X., and Tomizuka, M., 2012. "Decoupled disturbance observers for dual-input-single-output systems with application to vibration rejection in dual-stage hard disk drives". In Proc. 2012 ASME Dynamic Systems and Control Conf., and 2012 Motion & Vibration Conf., pp. 1544–1554.
- [16] Abramovitch, D. Y., and Franklin, G. F., 2002. "A brief history of disk drive control". *IEEE Control Syst. Mag.*, **22**(3), pp. 28–42.
- [17] Al Mamun, A., and Ge, S. S., 2005. "Precision control of hard disk drives". *IEEE Control Syst. Mag.*, **25**(4), pp. 14–19.
- [18] Jia, Q.-W., 2009. "Disturbance rejection through disturbance observer with adaptive frequency estimation". *IEEE Trans. Magn.*, **45**(6), June, pp. 2675–2678.
- [19] Zhou, K., and Doyle, J. C., 1998. *Essentials of robust control*. Prentice Hall New Jersey, Oct.
- [20] Scherer, C., Gahinet, P., and Chilali, M., 1997. "Multiobjective output-feedback control via LMI optimization". *IEEE Trans. Autom. Control*, **42**(7), July, pp. 896–911.
- [21] Boyd, S. P., El Ghaoui, L., Feron, E., and Balakrishnan, V., 1994. *Linear matrix inequalities in system and control theory*. Society for Industrial Mathematics.
- [22] Grant, M., and Boyd, S., 2011. CVX: Matlab software for disciplined convex programming, version 1.21. <http://cvxr.com/cvx>, Feb.
- [23] Guo, L., Martin, D., and Brunnett, D., 1999. "Dual-stage actuator servo control for high density disk drives". In Proc. 1999 IEEE/ASME International Conf. on Advanced Intelligent Mechatronics, pp. 132–137.
- [24] Al Mamun, A., Mareels, I., Lee, T., and Tay, A., 2003. "Dual stage actuator control in hard disk drive—a review". In The 29th Annual Conf. of the IEEE Industrial Electronics Society, Vol. 3, pp. 2132–2137.
- [25] Horowitz, R., Li, Y., Oldham, K., Kon, S., and Huang, X., 2007. "Dual-stage servo systems and

vibration compensation in computer hard disk drives". *Control Engineering Practice*, **15**(3), pp. 291–305.

- [26] Al Mamun, A., Guo, G., and Bi, C., 2007. *Hard disk drive: mechatronics and control*. CRC Press.

Appendix A: Proof of Theorem 1

From Eq. (13), under the stated conditions, the closed-loop characteristic polynomial comes from

$$\begin{aligned} 1 + P_1 C_1 + P_2 \frac{C_2 + (1 + \hat{P}_1 C_1) z^{-m_2} \hat{P}_2^{-1} Q_2}{1 - z^{-m_2} Q_2} &= 0 \\ \iff 1 + P_1 C_1 + P_2 C_2 - z^{-m_2} Q_2 - z^{-m_2} Q_2 P_1 C_1 \\ &+ z^{-m_2} Q_2 P_2 \hat{P}_2^{-1} + z^{-m_2} Q_2 P_2 \hat{P}_2^{-1} \hat{P}_1 C_1 = 0 \quad (34) \end{aligned}$$

If $P_i = \hat{P}_i$ then the two pairs of terms $(-z^{-m_2} Q_2, z^{-m_2} Q_2 P_2 \hat{P}_2^{-1})$ and $(-z^{-m_2} Q_2 P_1 C_1, z^{-m_2} Q_2 P_2 \hat{P}_2^{-1} \hat{P}_1 C_1)$ get canceled. However the canceled terms will still contribute to internal states. The actual closed-loop characteristic polynomial, with $P_i = \hat{P}_i$, is

$$\begin{aligned} D_{Q_2} N_{\hat{P}_2} \times \\ (D_{P_1} D_{P_2} D_{C_1} D_{C_2} + N_{P_1} N_{C_1} D_{P_2} D_{C_2} + N_{P_2} N_{C_2} D_{P_1} D_{C_1}) \end{aligned}$$

where $N_{(\cdot)}$ and $D_{(\cdot)}$ denote respectively the numerator and denominator of a transfer function. Notice that $D_{P_1} D_{P_2} D_{C_1} D_{C_2} + N_{P_1} N_{C_1} D_{P_2} D_{C_2} + N_{P_2} N_{C_2} D_{P_1} D_{C_1}$ is the characteristic polynomial for the baseline system. The internal stability follows readily from the assumptions.

Appendix B: Proof of Theorem 2

Consider first the general closed-loop system for DISO plants under perturbation, as shown in Fig. 20. Here \tilde{C}_i 's are the equivalent feedback controllers. To obtain the robust stability condition, we transform Fig. 20 to the generalized representation in Fig. 21, where

$$G = \frac{W \tilde{C} \hat{P}}{1 + \hat{P} \tilde{C}} = \frac{1}{1 + \hat{P}_1 \tilde{C}_1 + \hat{P}_2 \tilde{C}_2} \begin{bmatrix} W_1 \tilde{C}_1 \\ W_2 \tilde{C}_2 \end{bmatrix} \begin{bmatrix} \hat{P}_1 & \hat{P}_2 \end{bmatrix}. \quad (35)$$

From μ -analysis, the closed-loop system is stable w.r.t. the plant perturbations if and only if G is stable and the structured singular value of G satisfies: $\forall \omega, \mu_\Delta(G(e^{-j\omega})) < 1$. In Fig. 21, consider the smallest (in the sense of H_∞ norm) perturbation Δ such that the following stability boundary is attained:

$$\det(I + \Delta(e^{-j\omega})G(e^{-j\omega})) = 0. \quad (36)$$

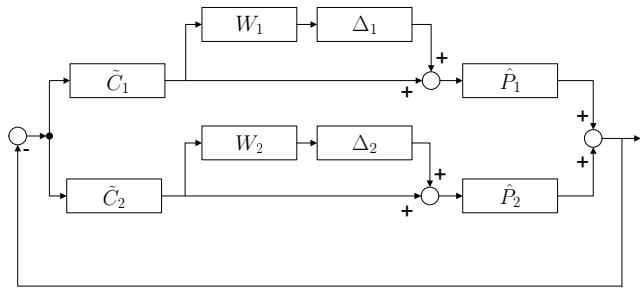


Fig. 20: General closed loop for perturbed DISO plants

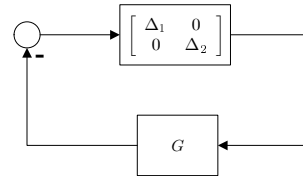


Fig. 21: Generalized block diagram of Fig. 20

Substituting $\Delta = \text{diag}\{\Delta_1, \Delta_2\}$ and Eq. (35) to Eq. (36) yields

$$\begin{aligned} \det(I + \Delta G) \\ = \det \left(I + \begin{bmatrix} \Delta_1 & 0 \\ 0 & \Delta_2 \end{bmatrix} \frac{1}{1 + \hat{P}_1 \tilde{C}_1 + \hat{P}_2 \tilde{C}_2} \begin{bmatrix} W_1 \tilde{C}_1 \\ W_2 \tilde{C}_2 \end{bmatrix} \begin{bmatrix} \hat{P}_1 & \hat{P}_2 \end{bmatrix} \right) \\ = 1 + \frac{\hat{P}_1 \Delta_1 W_1 \tilde{C}_1 + \hat{P}_2 \Delta_2 W_2 \tilde{C}_2}{1 + \hat{P}_1 \tilde{C}_1 + \hat{P}_2 \tilde{C}_2}, \quad (37) \end{aligned}$$

where the last equality has used the determinant identity $\det(I + AB) = \det(I + BA)$.

Combining Eq. (37) and Eq. (36), the minimum- H_∞ -norm perturbation is obtained when $|\Delta_1| = |\Delta_2| =: |\Delta_0|$ and the following equality holds

$$1 - \left| \frac{\hat{P}_1 W_1 \tilde{C}_1}{1 + \hat{P}_1 \tilde{C}_1 + \hat{P}_2 \tilde{C}_2} \right| |\Delta_0| - \left| \frac{\hat{P}_2 W_2 \tilde{C}_2}{1 + \hat{P}_1 \tilde{C}_1 + \hat{P}_2 \tilde{C}_2} \right| |\Delta_0| = 0.$$

By definition, the structured singular value is

$$\mu = \frac{1}{|\Delta_0|} = \frac{|\hat{P}_1 \tilde{C}_1| |W_1| + |\hat{P}_2 \tilde{C}_2| |W_2|}{|1 + \hat{P}_1 \tilde{C}_1 + \hat{P}_2 \tilde{C}_2|}. \quad (38)$$

When DDOB is in the feedback loop as shown in Fig. 6, $\tilde{C}_1 = C_1$ and $\tilde{C}_2 = C_{2,s}(C_2 + C_{2,p})$, where $C_{2,s}$ and $C_{2,p}$ are given by Eq. (10) and Eq. (11). After simplification, one can get the explicit form of Eq. (17).